Pinning, ordering, and dynamics of vortices in conformal crystal and gradient pinning arrays

D. Ray, C. Reichhardt, and C. J. Olson Reichhardt
Theoretical Division, Los Alamos National Laboratory, Los Alamos, New Mexico 87545, USA
(Received 1 August 2014; published 8 September 2014)

We numerically investigate magnetization, pinning, ordering, and dynamics of vortices interacting with pinning arrangements which have a density gradient. We focus on conformal crystal structures obtained by conformally transforming a spatially uniform periodic array, as well as nonconformal gradient structures and structures with quasiperiodic order. The conformal structures feature a density gradient and local ordering. Using magnetization simulations we find that conformal pinning arrays exhibit enhanced pinning compared to nonconformal gradient arrays as well as compared to random, periodic, and quasiperiodic arrays, for a broad range of fields. The effectiveness of conformal arrays arises from the continuum of length scales introduced into the arrays by the conformal transformation, allowing for a broad range of local commensuration effects. At higher vortex fillings above the range of conformal effectiveness, we show that a nonconformal rectangular gradient array exhibits strong pinning due to a novel commensuration effect and vortex ordering. Using transport simulations where vortices are driven along the gradient and at an angle to the gradient, we confirm the effectiveness of conformal pinning at increasing the critical current. For a rotated drive, the gradient arrays produce a strong vortex guidance effect in the direction perpendicular to the gradient.

DOI: 10.1103/PhysRevB.90.094502 PACS number(s): 74.25.Wx, 74.25.Uv

I. INTRODUCTION

One of the most important issues for many applications of type-II superconductors is understanding how to optimize the pinning of magnetic flux vortices, since the system becomes dissipative when vortices are in motion [1]. The applied current at which vortices depin is called the critical current J_c, and there has been intense research in tailoring the pinning in a superconductor so as to maximize J_c for either specific applied fields or for a broad range of fields. Beyond the direct application to superconductivity, vortex pinning and dynamics provide a very rich system for exploring collective ordering of particles on random or periodic substrates, as well as for studying nonequilibrium phenomena at depinning which arise in a variety of condensed matter systems, such as driven charge density waves [2], sliding Wigner crystals [3], atomic friction [4], adhesion [5], magnetic domain wall motion [6], and driven colloidal systems [7].

A widely used method for enhancing the pinning and critical current in superconductors is the creation of nanostructured artificial arrays of pinning sites [8–13], featuring a well-defined number of sites arranged in a desired configuration. These sites pin vortices effectively, but only a limited number of sites can be added to a sample since their creation causes local damage to the superconductor that decreases the material's current-carrying capacity. Therefore, it is of great importance to determine the optimal geometrical arrangement of a *fixed* number of pinning sites that generates the strongest pinning over the widest range of fields. In random site arrangements, where there is a distribution of interpin spacings, the closely spaced pins are inefficiently used due to strong short-range intervortex repulsion, while widely spaced pins permit easy flow of vortices between them [14]. Periodic pinning arrays such as triangular or square arrays, which avoid both these shortcomings, have been studied in detail; the pinning is enhanced compared to random arrays, but only near certain *commensurate* field values, where the number of vortices is an integer [8–13,15–17] or fractional [18,19] multiple of the number of pinning sites. At commensurability, ordered or partially ordered vortex arrangements form which can have various types of symmetries [9,15–19]; however, away from commensurability, the vortex structures are partially or totally disordered, allowing for the formation of weak spots and easy vortex flow channels which reduce the depinning threshold [9,15,18]. Rectangular pinning arrays that are periodic with two different length scales have been shown to produce anisotropic vortex structures and transport [20–24].

There have been a number of efforts to enhance the pinning in periodic arrays under noncommensurate conditions. Systematically diluting a triangular pinning array gives enhanced pinning not only at matching fields, but also at noninteger matching fields corresponding to what the integer matching fields for the nondiluted array would have been [25–30]. Other studies showed that the addition of some disorder to a triangular pinning lattice enhances the pinning at incommensurate fillings, but at the cost of reducing the maximum pinning at the integer matching fields [31]. Asymmetric system geometries, such as funnel geometries [32–34] or periodic constriction geometries [35] which utilize vortex jamming, produce new types of commensurability effects. Vortex artificial ice states can be created using superlattices of square pinning arrangements [36–38], and exhibit strong matching at certain noninteger fields. Composite pinning lattices based on intermeshed periodic arrays have also been created [39–41].

Another approach to pinning enhancement is the use of pinning structures that combine aspects of periodicity and disorder. Studies of quasiperiodic arrays where pinning sites were placed at the vertices of a Penrose tiling [42–48] revealed novel noninteger matching conditions, and showed that the overall pinning can be enhanced over periodic triangular pinning arrays below the first matching field [42,43,45,47].

Despite these efforts, pinning arrays which rely on commensuration effects have continued to possess the fundamental drawback of only providing enhanced pinning near certain field values, rather than over a broad range of field. In an

effort to overcome this shortcoming, a new type of pinning geometry, known as a conformal crystal pinning array, was recently proposed [49]; an example of such an array is shown in Fig. 1(b). A conformal crystal is constructed by performing a conformal, or angle-preserving, transformation upon a uniform lattice structure such as a hexagonal array, producing a new structure which preserves the *local* ordering of the original array but now exhibits a density gradient in one direction [49,50]. Conformal crystals were first observed as the approximate ground state structure of a set of repulsively interacting magnetic spheres restricted to move in two dimensions and subjected to a gravitational potential; the distinctive arching appearance of the resulting structure inspired the whimsical nickname of "gravity's rainbow" [50]. In vortex simulations, conformal pinning arrays produced enhanced pinning compared to an equivalent number of pinning sites arranged randomly with uniform density over a wide range of applied fields, with the enhancement persisting until the applied field was increased beyond the maximum local pinning density present in the array [49]. The conformal array also outperformed uniform periodic arrays except in the immediate vicinity of the matching field. A random array with a density gradient produced pinning only marginally better than a nongradient random array and substantially worse than the conformal array, indicating that the preservation of local order was as vital to the conformal array's performance as was the introduction of a gradient. The enhancement was observed both in flux gradient-driven simulations [49], where the vortices enter or exit the system from the edges, and in current-driven simulations [49,51], where the vortex density is fixed and the vortices are driven across the sample with a uniform Lorentz force. Two subsequent experiments confirmed the enhanced pinning in conformal arrays. In the first [52], conformal pinning arrays displayed enhanced critical currents over uniform periodic pinning arrays except in the vicinity of certain matching fields. In the second [53], conformal pinning arrays showed decreased magnetoresistance in transport experiments compared to periodic or diluted periodic structures with the same number of pinning sites.

Pinning arrays with a density gradient not produced by a conformal transformation have also been investigated. A pinning array consisting of concentric rectangular "rings" of pinning sites with a gradually increasing separation between the rings was fabricated and shown to exhibit enhanced pinning compared to a periodic pinning array [54]. Additionally, there have been numerical studies of pinning arrays arranged in circular hyperbolic tessellation structures so that the pinning sites have a gradient [55]; however, these studies did not include comparisons with periodic or random pinning arrays to check whether the hyperbolic array produces enhanced pinning over the other geometries.

In this work, we use molecular dynamics simulations to study magnetization, depinning, ordering, and dynamics of vortices in systems with various types of pinning arrays featuring a density gradient. We investigate the effect of different local orderings in conformal crystal arrays by considering transformed versions of hexagonal, square, quasiperiodic, and Archimedean [56,57] lattices. We also consider two nonconformal systems, a rectangular pinning array with a one-dimensional (1D) gradient, and a random pinning arrangement with a density gradient. This paper is organized as follows: In Sec. II, we describe how conformal arrays are created and enumerate the various pinning arrays which will be analyzed. In Sec. III, we explain our physics model and the types of simulations we perform. In Sec. IV, we show the results of magnetization simulations, demonstrating that conformal pinning arrays produce enhanced pinning over nonconformal gradient arrays over a wide range of applied fields, as well as over arrays of uniform density such as the quasiperiodic Penrose array or periodic arrays (aside from a narrow range around matching fields). In Sec. V, by examining the pattern of occupied pinning sites as the field is increased, we show that the effectiveness of conformal arrays is due to a *local* commensuration effect which is an extension of the global matching exhibited by uniform pinning arrays: because the conformal transformation introduces a continuously changing lattice constant into the array, the vortex lattice can progressively match with different slices of the array as the number of vortices is increased. Consequently, we find that the particular type of local order present is relatively unimportant in determining the effectiveness of conformal pinning arrays, as long as some type of ordering is present that would give a matching effect in a uniform array. We also use local commensuration to explain the maximum effective field value for conformal arrays. At higher fields well above this value, we show in Sec. VI that a rectangular gradient pinning array gives enhanced pinning over the conformal arrays due to a novel commensuration effect which gives rise to ordered vortex chain structures. In Sec. VII, we examine current-driven vortex dynamics for vortices driven along the gradient direction as well as at varied angles with respect to the gradient. We find that in general, conformal pinning arrays reduce vortex motion compared to the other arrays, over the full range of drive angles. Compared to the random and rectangular gradient arrays which exhibit channels of easy vortex flow, the arching structure of the conformal arrays prevents the formation of such channels for any choice of drive angle. Additionally we find that many gradient arrays have a pronounced vortex guidance effect, where vortices move much more easily perpendicular to the gradient than along the gradient. Finally, in Sec. VIII, we present our conclusions.

II. GRADIENT PINNING ARRAYS

A. Conformal arrays

Conformal transformations are a well-studied topic from complex analysis [58]. An analytic function $w = f(z)$ maps two infinitesimal vectors originating from the same point in the z plane with angle θ between them to two new vectors in the w plane separated by the same angle. We use this property to transform an ordered structure into one which remains locally ordered but which is distorted on a global scale.

In this work, we allow the transformation

$$w = \frac{\pi}{2\alpha} + \frac{1}{i\alpha}\ln(i\alpha z)$$

(where α is a constant which we set to $\pi/36$) to act on a semiannular section of the z plane specified by $\mathrm{Im}z \geqslant 0$ and $r_{\mathrm{in}} \leqslant |z| \leqslant r_{\mathrm{out}}$ for some choice of r_{in} and r_{out}. This transformation maps radial lines in the z plane to vertical

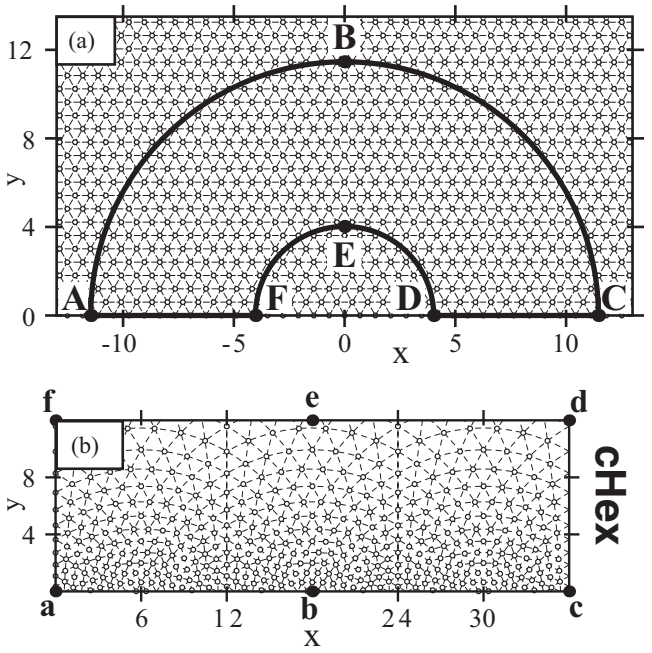

FIG. 1. (a) A semiannular section of a uniform hexagonal lattice. (b) Effect of a conformal transformation upon the region in (a). The resulting structure (conformal hex or "cHex") has local hexagonal ordering and a density gradient. See text for details of the transformation. Points A-F in (a) are mapped to points a-f in (b) by the transformation.

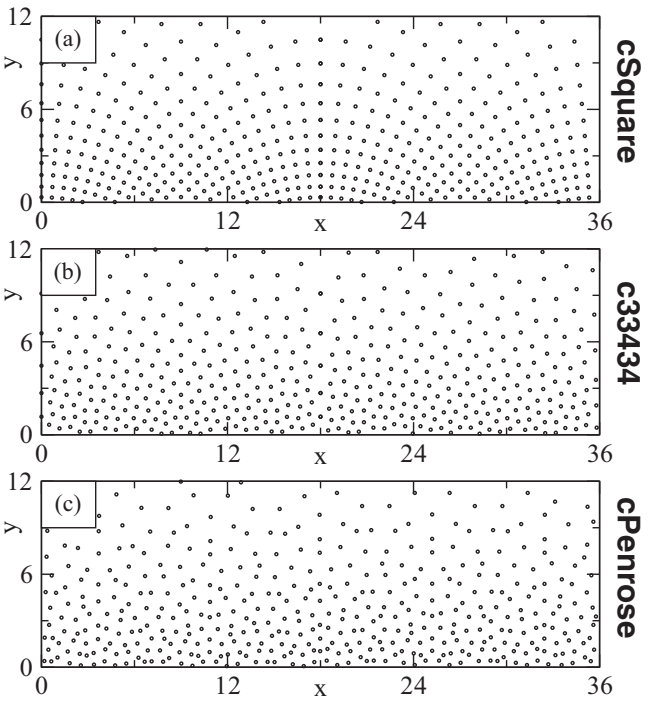

FIG. 2. Conformally transformed versions of various uniform (non-gradient) structures: (a) square lattice; (b) Archimedean 33434 lattice (a periodic tiling of the plane using squares and triangles); (c) 5-fold Penrose tiling using thin and thick rhombs.

lines in the w plane, and circular arcs centered at the origin to horizontal lines. Consequently, the semiannular region **ABCDEF** is mapped to the rectangle **abcdef**, as shown in Fig. 1. The circular arcs in the z plane are increasingly stretched by the transformation as their radial coordinate decreases: fixing $\alpha r_{\text{out}} = 1$, arc **ABC** has the same length as line **abc**, while arc **DEF** is stretched to the same length as lines **def** and **abc**. This increasing stretch causes an ordered structure with uniform density, such as the hexagonal lattice shown in Fig. 1(a), to be mapped to a structure with a density gradient, as shown in Fig. 1(b). The local ordering of the original structure is preserved due to the conformal nature of the mapping: each site in the transformed lattice retains its six nearest neighbors.

The conformally transformed hexagonal structure was studied in previous work [49,51], where it was termed a "conformal pinning array" or "CPA." Since in the present work we also consider other types of local order, we here refer to this array as a "conformal hex" array, or "cHex" for short. Figure 2 illustrates conformal arrays with other types of local order. In Fig. 2(a), a transformed square lattice exhibits local fourfold order. We refer to this tiling as "conformal square" or "cSquare." Figure 2(b) shows the transformed version of a so-called "Archimedean 33434" array. Archimedean tilings of the plane are periodic tilings created using two or more types of regular polygon. Several such tilings exist [57]; here we consider a particular type, 33434, composed of squares and triangles. A uniform pinning array based on such a tiling has been studied extensively [56]. We refer to the transformed version as "conformal 33434" or "c33434." Finally, Fig. 2(c) shows the transform of a Penrose tiling with approximate fivefold symmetry, constructed using thin and thick rhombs [59]. Pinning arrays based upon such Penrose tilings have been simulated previously [42]; here, we consider transformed Penrose arrays ("conformal Penrose" or "cPenrose"), as well as a uniform (untransformed) Penrose array. The uniform version of each array type will be referred to, when required, as "uHex," "uSquare," "u33434," and "uPenrose."

All pinning arrays fit into a rectangular region of dimension $36\lambda \times 12\lambda$, where λ is the London penetration depth, and have a nominal average density of pinning sites equal to $\bar{\rho}_p = 1.0/\lambda^2$ (i.e., each array contains approximately 432 pins, with small deviations on the order of 1% due to boundary effects.) This density can be obtained through appropriate choices of the parameter r_{in} and the lattice constant of the original uniform lattice. The local pinning density varies from a maximum of $\rho_p^{\text{loc}} = 2.0/\lambda^2$ to a minimum of $\rho_p^{\text{loc}} = 0.3/\lambda^2$.

B. Arrays produced by other methods

The conformal arrays described above all have the common features of local ordering and a density gradient. The local pinning density (or equivalently, the local lattice constant) varies fairly smoothly through the array due to the continuous nature of the conformal transformation. In order to determine the relative importance of each of these two features in maximizing the effectiveness of the pinning, we consider two other array types.

The first alternative array is shown in Fig. 3(a) and consists of a rectangular pinning array with a lattice constant that varies in the gradient direction so as to approximate the density profile

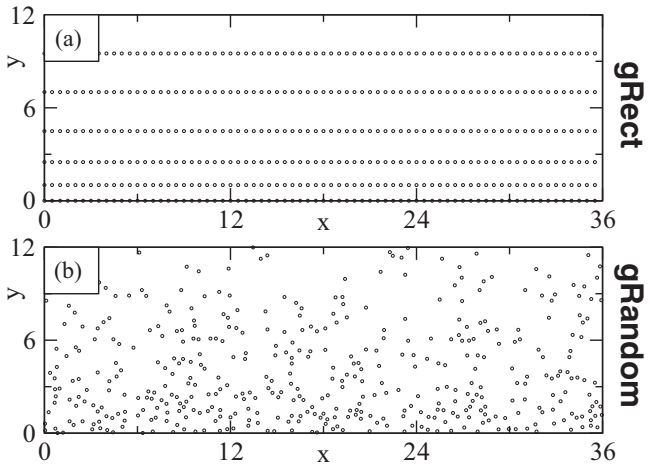

FIG. 3. Gradient pinning arrays not formed by a conformal transformation. (a) A rectangular gradient pinning array, consisting of rectangles stretched and compressed in one dimension. (b) Random (disordered) pinning with a density gradient matching the conformal arrays.

of the conformal arrays as closely as possible. We call this array "rectangular with gradient," or "gRect." The gRect array differs from the conformal arrays in two respects: (i) the lattice constant does not vary smoothly through the array, and (ii) the original uniform rectangular array from which the gradient array was constructed does not exhibit a commensuration peak. The importance of this second property will be explained in Sec. V.

The second alternative array, shown in Fig. 3(b), has a density gradient matching that of the conformal arrays, but the pinning sites are arranged randomly subject only to this constraint, so that all local ordering is eliminated. This array, called "random with gradient" or "gRandom," was studied in earlier work [49] and found to be only minimally more effective than uniform random pinning. Thus, we use the gRandom array to establish a baseline of minimum effectiveness for pinning arrays with a density gradient. Notice that this array type can be generated either by using the desired density profile as a bias when generating pinning locations, or by conformally transforming a uniform random array; the transformation does not add order where none was originally present.

III. SIMULATION AND SYSTEM

We employ two types of simulation geometries in this work. The first is a flux gradient-driven geometry [49,55,56,60,61] where we apply a slowly varying magnetic field to a superconductor with pinning sites and calculate the resulting magnetization loops. Specifically, we consider a two-dimensional (x-y) slice of a bulk superconductor subjected to an applied magnetic field $\mathbf{H} = H\hat{\mathbf{z}}$. We treat the resulting vortices in the material as perfectly stiff and use the London limit in which the vortices are assumed to be pointlike in the x-y plane. We measure all lengths in terms of the penetration depth λ. Our system is a square of side $L = 36\lambda$ with periodic boundary conditions in both the x and y directions. As shown in Fig. 4(a),

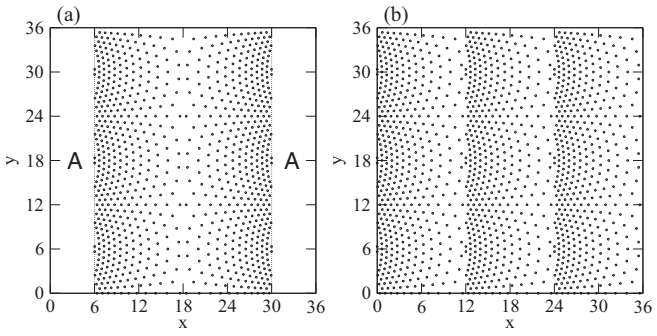

FIG. 4. Pinning geometries for both types of simulations, illustrated using the cHex array. In each case, the sample is periodic in the x and y directions. (a) Magnetization simulation geometry. The pinned region representing the superconducting sample extends from $x = 6\lambda$ to $x = 30\lambda$. Two copies of a gradient pinning array are placed in the pinned region, with their sparse sides facing each other. Vortices and antivortices are added to the unpinned outer regions labeled "A," which represent an applied external field. (b) Transport simulation geometry. The pinned region spans the entire simulation box. Three copies of a gradient pinning array are placed in the box, all facing the same direction. Vortices are placed randomly and annealed before the simulation begins; during the simulation, a steadily increasing drive is applied.

the pinning is added in a region extending from $x = 6\lambda$ to 30λ which represents the superconducting sample. Vortices and antivortices are added in the unpinned external regions labeled "A" to the left and right of the sample; the vortex density in these regions represents the applied external magnetic field H. For pinning arrays with a gradient, we place two copies of the array in the sample region, oriented so that their dense sides face the external regions, while their sparse sides face each other. The geometry and system size described here were previously shown to be sufficiently large to accurately model both magnetization curves and vortex ordering for conformal crystal pinning arrays [49], periodic pinning arrays [49,56,61], and random pinning [49,55,60].

At a given time during the simulation, the system contains a total of N_v vortices and antivortices; this quantity changes as the external field is changed over the course of the simulation. The equation of motion for vortex i is given by

$$\eta \frac{d\mathbf{R}_i}{dt} = \mathbf{F}_i^{vv} + \mathbf{F}_i^{p}. \tag{1}$$

Here $\mathbf{R}_i$ is the location of the vortex and η is the damping constant which we set to unity. The vortex-vortex interaction force is

$$\mathbf{F}_i^{vv} = \sum_{j \neq i} s_i s_j F_0 K_1(R_{ij}/\lambda)\hat{\mathbf{R}}_{ij},$$

where $F_0 = \phi_0^2/2\pi\mu_0\lambda^3$, $\phi_0 = h/2e$ is the elementary flux quantum, μ_0 is the permittivity of free space, K_1 is the modified Bessel function, $R_{ij} = |\mathbf{R}_i - \mathbf{R}_j|$, and $\hat{\mathbf{R}}_{ij} = (\mathbf{R}_i - \mathbf{R}_j)/R_{ij}$. We measure all forces in terms of F_0. For computational efficiency, we truncate the interaction force beyond $R_{ij} = 6\lambda$, which is a good approximation since $K_1(x)$ falls off exponentially for large x. Vortices repel each other, as do antivortices, while a vortex attracts an antivortex; to represent

this interaction, we use the sign prefactor s_i which is $+1$ for a vortex and -1 for an antivortex. If a vortex and an antivortex approach each other within a distance smaller than 0.3λ, they are both removed from the system to simulate an annihilation event. Most of our simulations involve only vortices; we use antivortices only to generate full magnetization loops, described below. The pinning arises from N_p nonoverlapping traps each represented by a truncated parabolic pinning potential, so that the pinning force is given by

$$\mathbf{F}_i^p = \sum_{k=1}^{N_p} \left(F_p R_{ik}^p / R_p\right) \Theta\left[\left(R_p - R_{ik}^p\right)/\lambda\right] \hat{\mathbf{R}}_{ik}^p,$$

where R_k^p is the location of pinning site k, $R_{ik}^p = |\mathbf{R}_i - \mathbf{R}_k^p|$, $\hat{\mathbf{R}}_{ik}^p = (\mathbf{R}_i - \mathbf{R}_k^p)/R_{ik}^p$, Θ is the Heaviside step function, the pinning radius R_p is set to 0.12λ, and F_p specifies the maximum strength of the pinning force.

To construct a full magnetization loop, we begin with an empty sample and gradually add vortices to the unpinned regions marked "A" in Fig. 4(a). As the vortex density increases in the unpinned region, vortices are pushed into the sample due to the intervortex repulsion. We continue to add vortices until reaching the desired maximum value of the external magnetic field H; then we begin to add antivortices. As these annihilate with vortices, H decreases back to zero and then becomes negative as the unpinned region fills with antivortices. Finally, we add vortices again to bring H back up to zero. As the simulation progresses, we record the magnetization

$$M = -\frac{1}{4\pi V} \int dV\,(H - B)$$

where V represents the sample area, H is the average vortex density over the unpinned region, and B is the (position-dependent) vortex density in the sample region. According to the Bean critical state model [62], the width of the magnetization loop is proportional to the critical current J_c. This width can be determined using only the first quarter of the magnetization loop, and so in many of our simulations, we generate only a quarter loop instead of a full loop by using vortices to raise the external field up to a maximum value and then halting the simulation.

The second simulation geometry we consider is current driven rather than flux gradient driven, and is similar to that used in previous studies of current-driven vortex dynamics in pinned superconductors [48,63,64]. We add an additional force term $\mathbf{F}^d = F_d F_0 \hat{n}$ to the vortex equation of motion in Eq. (1) to represent the Lorentz force exerted by an applied external current $\mathbf{J}$; here $\hat{n}$ is a constant unit vector in the x-y plane. This force affects all vortices uniformly. For the purposes of an initial anneal, we also add a term $\mathbf{F}_i^T$ representing thermal Langevin kicks to Eq. (1), where $\mathbf{F}_i^T$ has the properties $\langle \mathbf{F}_i^T \rangle = 0$ and $\langle \mathbf{F}_i^T(t) \mathbf{F}_j^T(t') \rangle = 2\eta k_B T \delta_{ij} \delta(t - t')$. We modify the system geometry to measure transport properties by removing the external unpinned regions and employing a pinning configuration composed of three copies of a given pinning array facing in the same direction and filling the entire simulation box, as shown in Fig. 4(b). To initialize the system we place N_v vortices in randomly chosen nonoverlapping locations in the simulation box, and perform a simulated anneal from $T = 3.0$ to $T = 0$ while holding $F_d = 0$ before beginning our measurement. Throughout a transport simulation, N_v is held constant in order to model a constant magnetic field level. We increase the magnitude of the current-induced driving force F_d in small increments of size $\delta F_d = 5 \times 10^{-4}$ and spend 500 simulation time steps at each value of F_d in order to avoid any transient behavior. We measure the average vortex velocity in the x and y directions as a function of drive: $\langle V_x \rangle = (1/N_v) \sum_{i=1}^{N_v} \mathbf{v}_i \cdot \hat{x}$ and $\langle V_y \rangle = (1/N_v) \sum_{i=1}^{N_v} \mathbf{v}_i \cdot \hat{y}$. The vortex velocity is proportional to the voltage response, so the velocity-force curve we generate is comparable to an experimentally measurable current-voltage curve.

IV. MAGNETIZATION

In Fig. 5 we plot the full magnetization loops M vs H/H_ϕ, where H_ϕ is the matching field at which there is one vortex per pinning site, for the conformal pinning array cHex from Fig. 1, the nonconformal gradient arrays gRect and gRandom from Fig. 3, and a uniform random pinning array. For weak pinning sites with $F_p = 0.2$, Fig. 5(a) shows that the conformal array provides enhanced pinning compared to the other arrays over the entire range of field, as indicated by the fact that the magnetization loop is widest for the cHex array. The rectangular gradient arrays gRect and cHex have similar values of M up to $H/H_\phi = 1.0$, but for higher H/H_ϕ the conformal array is clearly the most effective at pinning the vortices. The difference between the conformal and random arrays becomes more pronounced when the pinning strength is increased, as is apparent for $F_p = 0.55$ in Fig. 5(b). The ordered gRect array shows slightly stronger pinning than cHex for $H/H_\phi < 1.0$, but falls off dramatically above that value. These effects are even more pronounced for $F_p = 0.9$, shown in Fig. 5(c). The difference between the uniform random and random gradient arrays increases with increasing F_p, but the mere addition of a gradient is not sufficient to give magnetization values that are anywhere close to as large as those obtained with the cHex array, particularly for higher values of H/H_ϕ. The effectiveness of the conformal array persists up to a field $H/H_\phi = 2.0$ before beginning to decline, and the critical current for cHex remains higher than that of gRect up to $H/H_\phi = 2.5$. Above $H/H_\phi = 1.75$ a new peak in M begins to emerge for the gRect sample with strong pinning; this feature will be treated in more detail in Sec. VI. We note that experiments in thin-film superconductors with through-hole pinning sites should exhibit strong pinning behavior equivalent to large values of F_p [52]. These results show the superiority of conformal gradient pinning over other types of gradient pinning, and also over random pinning of any sort. In previous work [49] we have already shown enhanced pinning for a conformal array compared to uniform periodic arrays over a broad range of fields, apart from certain narrow field ranges corresponding to matching conditions.

We next turn to Penrose pinning arrays, since these have been claimed [42,47] to also provide broadly effective pinning. The previous studies suffered from several drawbacks, such as a small sample and array size which diminishes any actual effect of the array's structure upon pinning effectiveness, the use of fractional pin occupancy as a proxy for critical current,

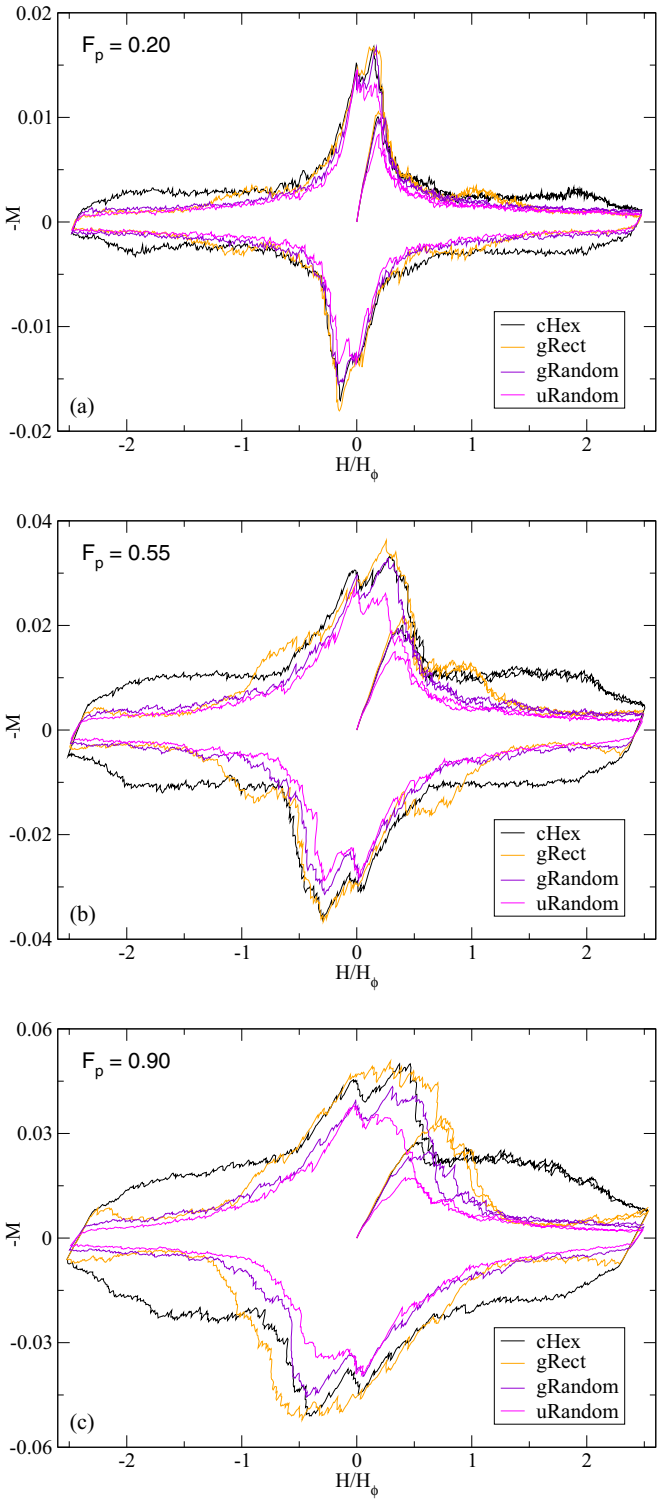

FIG. 5. (Color online) Full magnetization M vs external magnetic field H/H_ϕ loops for the conformal cHex array (outer loop), the nonconformal gRect and gRandom arrays (center loops), and uniform random pinning uRandom (inner loop), with $F_p =$ (a) 0.2, (b) 0.55, and (c) 0.9. The conformal array shows enhanced pinning over the other arrays in each case, and this is most noticeable when $|H/H_\phi| > 1.0$.

and most importantly a lack of comparisons to other pinning structures besides triangular. Here, we compare a Penrose array

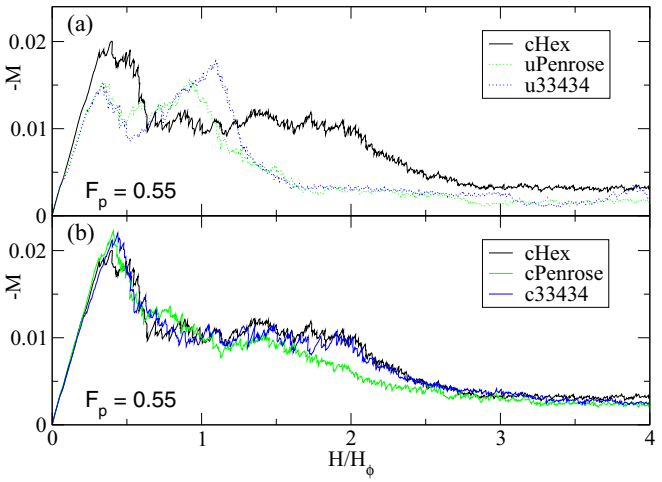

FIG. 6. (Color online) Magnetization M vs H/H_ϕ for cHex array (top right) compared to various arrays with two length scales in samples with $F_p = 0.55$. (a) Uniform 33434 (dotted blue, bottom right) and uniform Penrose (dotted green, center right); (b) conformal 33434 (solid blue, center right) and conformal Penrose (solid green, bottom right).

generated from a tiling with approximate fivefold symmetry, composed of thin and thick rhombs, to a conformal array. The magnetization curves for the uniform Penrose array with $F_p = 0.55$ in Fig. 6(a) show a matching peak near $H/H_\phi = 1.0$, similar to that found for a uniform periodic array. Away from the matching field, the magnetization drops off rapidly, again similar to the behavior of a periodic array. The magnetization of the cHex array is lower than that of the uPenrose array around the matching field, but is higher everywhere else. In particular, the cHex array gives a large enhancement of the magnetization up to and slightly beyond $H/H_\phi = 2.0$.

These results suggest that the quasiperiodic nature of a Penrose array is relatively unimportant as far as pinning effectiveness is concerned, and in fact its behavior is comparable to that of strictly periodic pinning structures. Since the Penrose tiling employs two different types of tiles giving rise to multiple length scales in the pinning structure, we use as a comparison a periodic tiling known as Archimedean 33434, which also uses two types of tiles, and which has been studied in the context of vortex pinning [56,57]. In Fig. 6(a) we show that the magnetization of the uniform 33434 array is in fact broadly similar to that of the uniform Penrose array, with a sharp matching peak in M at $H/H_\phi = 1$ followed by a rapid falloff.

Next, in order to examine the role of local order in conformal arrays, we consider the conformally transformed versions of the Penrose and Archimedean arrays which were shown in Fig. 2. We plot magnetization curves for these arrays in Fig. 6(b). Two behaviors are apparent. First, comparing the uniform arrays in Fig. 6(a) to their conformally transformed versions in Fig. 6(b), we see that the conformal transformation improves an array's performance over a broad range of field at the cost of eliminating the original matching peak at $H/H_\phi = 1$. Second, we find from Fig. 6(b) that even though vortices naturally arrange themselves in a hexagonal lattice

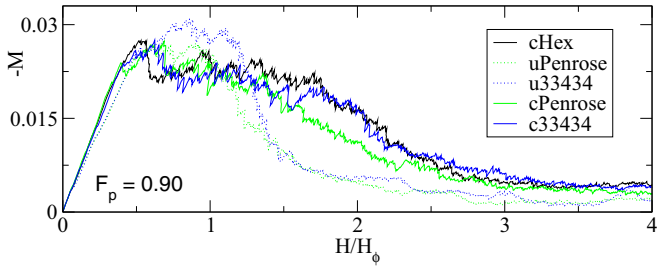

FIG. 7. (Color online) Magnetization M vs H/H_ϕ for cHex array (top right) compared to various arrays with two length scales in samples with $F_p = 0.90$: uniform 33434 (dotted blue, lower left), uniform Penrose (dotted green, lower right), conformal 33434 (solid blue, upper middle right), and conformal Penrose (solid green, center right).

in the absence of pinning, local hexagonal ordering is *not* necessary to obtain an effective conformal array: the c33434 array works as well, and the cPenrose array almost as well, as the cHex array at enhancing pinning.

To verify that these results are robust, we repeat our measurements in samples with an increased pinning strength of $F_p = 0.90$. As shown in Fig. 7, the magnetization curves retain all of the behaviors described above. In particular, we confirm that conformal arrays work better than uniform arrays in each case, and that their performance does not depend sensitively on the type of local order present in the original untransformed array. To further test this, a future study could compare cHex and cSquare arrays in magnetization loops which extend up to the third matching field, since a uniform square array has a commensuration peak at the second matching field but not the third, while the uniform triangular array has the opposite response.

V. LOCAL COMMENSURATION EFFECT IN CONFORMAL PINNING ARRAYS

In order to better understand how the structure of conformal arrays contributes to their enhanced pinning effectiveness over a broad range of field, and also what determines the limits of this range, we image the distribution of occupied pins as the field is increased. We take as our model system the cHex array with $F_p = 0.55$. In Fig. 8 we show three snapshots of the occupied pinning sites at different field values, where we find vertical bands in which all the pinning sites are filled. The location of these bands moves outwards towards the left and right edges of the sample as the field increases. This is seen more clearly in Fig. 9, where we plot the fraction of occupied pins $P_{\rm occ}(x)$ averaged over the vertical direction y as a function of horizontal position x for several different values of H/H_ϕ. Here $x = 18$ denotes the center of the pinned region, while the sample edges are at $x = 6$ and $x = 30$. For $H/H_\phi = 1.09$ in Fig. 9(b), we highlight two occupancy peaks in $P_{\rm occ}(x)$ near $x = 11$ and $x = 25$. These peaks correspond to the bands mentioned above, and signify areas where the vortex lattice *locally* matches with the pinning. This matching is distinct from the usual matching effect in a uniform pinning array which is global and occurs throughout the entire array. As H/H_ϕ increases, Figs. 9(c)–9(g) show that the occupancy

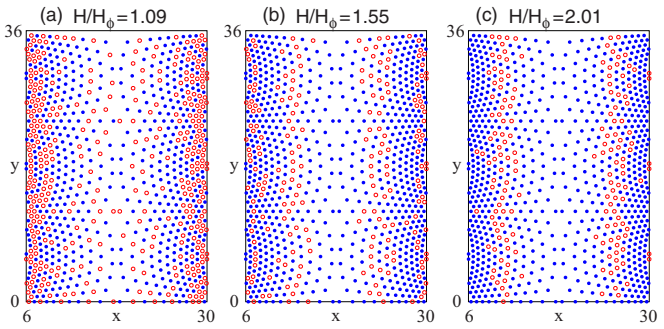

FIG. 8. (Color online) Occupied and empty pinning sites in a cHex array with $F_p = 0.55$, at H/H_ϕ= (a) 1.09, (b) 1.55, and (c) 2.01. Filled circles (blue): occupied pins; open circles (red): unoccupied pins. Pin sizes have been exaggerated for clarity. The occupied pinning sites form vertical bands that move toward the sample edges with increasing field.

peaks move toward the sample edges. This occurs because at matching, the vortex density must match the pinning density; thus, as the vortex density increases, the matching region must

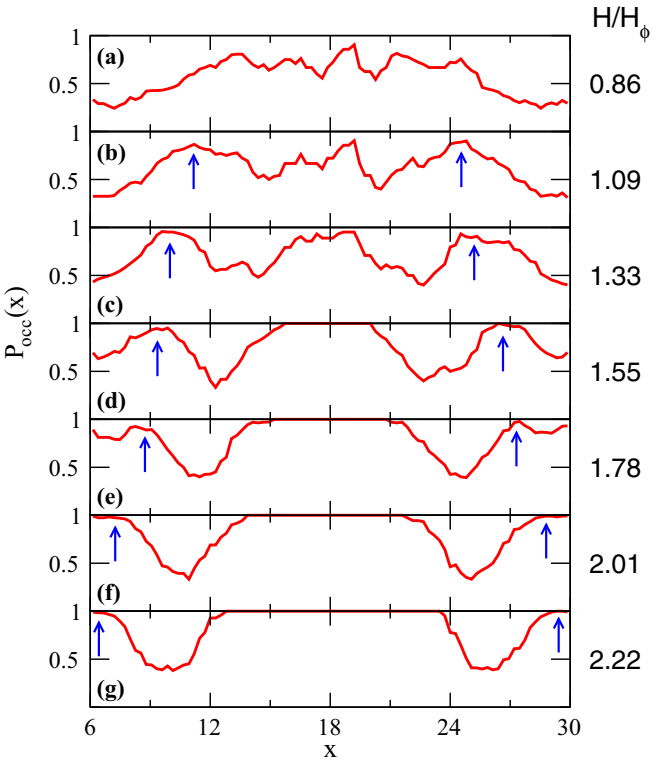

FIG. 9. (Color online) The spatial distribution of the fraction of occupied pins $P_{\rm occ}(x)$, averaged over the y direction, versus x position for the cHex array with $F_p = 0.55$ at H/H_ϕ= (a) 0.86, (b) 1.09, (c) 1.33, (d) 1.55, (e) 1.78, (f) 2.01, and (g) 2.22. The arrows in panels (b)–(g) highlight local regions of very high pin occupancy, indicating that the vortex lattice is locally commensurate with the pinning in these regions. As H/H_ϕ increases, the matching regions move toward the sample edges where the pinning density is greater. At the extreme edges of the sample the maximum local pinning density is $\rho_p^{\rm loc} = 2.0/\lambda^2$.

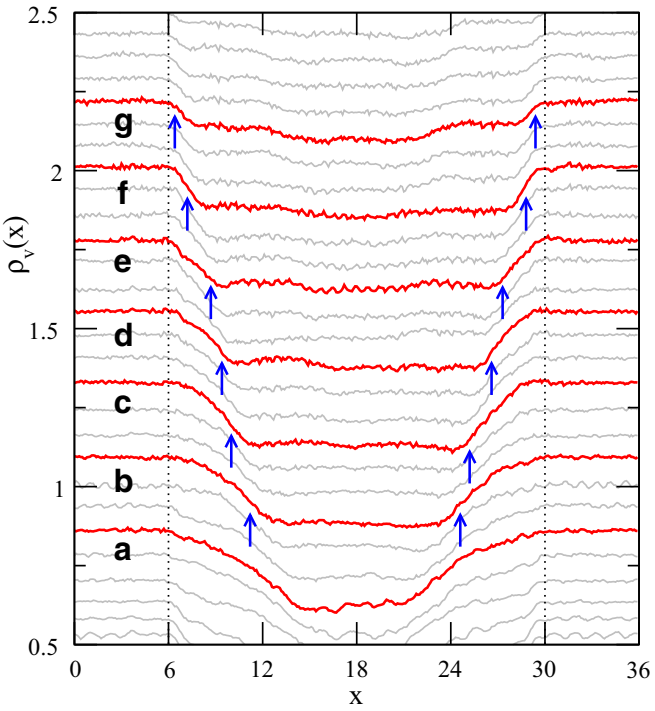

FIG. 10. (Color online) Vortex density ρ_v vs x position for the cHex array with $F_p = 0.55$ as the external field is gradually increased. Dotted lines indicate the sample edges; the sample extends from $x = 6\lambda$ to $x = 30\lambda$ as shown in Fig. 4(a). The value of H/H_ϕ for each curve is indicated by the average y value in the external regions $x < 6\lambda$ and $x > 30\lambda$. The lowest curve has $H/H_\phi = 0.52$, the highest curve has $H/H_\phi = 2.50$, and there is an interval of 100 added vortices, or $\delta H/H_\phi \approx 0.077$, between illustrated curves. Profiles in red correspond to the magnetic field values shown in Fig. 9; the letters indicate the corresponding panel in Fig. 9. Blue arrows point to the same locations as the arrows in Fig. 9 which show regions of high pin occupancy.

shift to the denser pinning regions that are closer to the edges of the sample. We also observe dips in $P_{\rm occ}(x)$ adjacent to the peaks, on the sides closer to the center of the sample. These dips arise due to the mismatch between vortices and pins once the commensuration peak has passed, with interstitial vortices forcing vortices out of the pinning sites. The migration of the local matching peaks continues as the field increases until the peaks reach the maximally dense pinning regions at the sample edges. For the conformal arrays we use in this work, the maximum local pinning density is $\rho_p^{\rm loc} = 2.0$, so we expect that once the vortex density ρ_v exceeds this value by a non-negligible amount, local matching will no longer be possible. In Fig. 9(g) where the external field has increased to $H/H_\phi = 2.22$, the matching regions have reached the edges of the sample and cannot move any further. Figure 6 shows that the effectiveness of the pinning of the cHex array falls off above this field value.

The vertical bands of occupied pins act as walls hindering vortices from flowing between the outer region and the inner region. These effective walls can maintain a large difference in vortex densities between these regions, leading to a large value of M. This is illustrated in Fig. 10, where we plot the vortex density ρ_v averaged over y as a function of horizontal position x as the field is increased. The field profiles have a double-slope, non-Bean-like shape as noted in previous work [49]. The high-slope regions where the vortex density changes rapidly are precisely the regions in which we find bands of occupied pins. We show this by drawing arrows pointing to the labeled highlighted profiles in Fig. 10 at the same locations where they appear in the corresponding pin occupancy plots in Fig. 9; these arrows clearly track the high-slope profile regions. The high-slope regions move towards the edges of the sample as the field increases, and first touch the edges at $H/H_\phi = 2.0$. Above this field, the high-slope regions begin to disappear since local matching can no longer occur, the vortex density equilibrates between the sample and the outside, and there is a corresponding drop in M as seen for cHex in Fig. 6.

In Fig. 11 we summarize the key characteristics of conformal arrays which produce the enhanced pinning. Although the data presented in the above discussion of local commensuration was from the cHex array, the local commensuration mechanism does not require hexagonal ordering; in fact, any local ordering that exhibits matching phenomena should be similarly effective. To show this, we first examine which array types are capable of exhibiting matching phenomena. Figure 11(a) shows the spatially averaged fraction of occupied pinning sites P vs H/H_ϕ for *uniform* arrays of the hexagonal, square, Penrose, 33434 (Archimedean), rectangular, and random type. The hexagonal, square, and 33434 arrays have a pronounced peak in $P_{\rm occ}$ just above $H/H_\phi = 1.0$, indicating that they exhibit robust matching. The Penrose array shows weaker matching, while the random and the rectangular arrays do not exhibit matching at all. In Fig. 11(b) we plot M versus H/H_ϕ for the corresponding conformal or gradient arrays, cHex, cSquare, cPenrose, c33434, gRect, and gRandom. As expected from the arguments above, we find that the conformal versions of the hexagonal, square, and 33434 arrays all show highly enhanced pinning up to $H/H_\phi = 2.0$, resulting from robust local matching. The conformal Penrose array shows a weaker pinning enhancement since the commensuration effects in the original uniform Penrose array are weaker. The rectangular and random gradient arrays give much lower magnetization values than the other arrays because they are not conformal and do not exhibit a local matching mechanism. We conclude that for *any* uniform array with a well-defined matching condition, the corresponding conformal array will exhibit enhanced pinning over a broad range of fields. For the conformal arrays we consider, this field range is $0.6 < H/H_\phi < 2.0$, and it is determined by the local pinning density $\rho_p^{\rm loc}(x)$ which we plot in Fig. 11(d) for the conformal hex lattice shown in Fig. 11(c). (Other conformal arrays will have similar density profiles.) At the minimum external field $H/H_\phi = 0.6$, the local matching occurs at the minimum density region in the center of the sample, where $\rho_p^{\rm loc} = 0.3$. The local matching moves toward the sample edges as the field increases, until for $H/H_\phi = 2.0$ the matching reaches the sample edges where the pinning density is also $\rho_p^{\rm loc} = 2.0$. Future experimental studies can determine the maximum steepness of the pinning gradient which will still permit local matching to occur and be effective at enhancing the pinning.

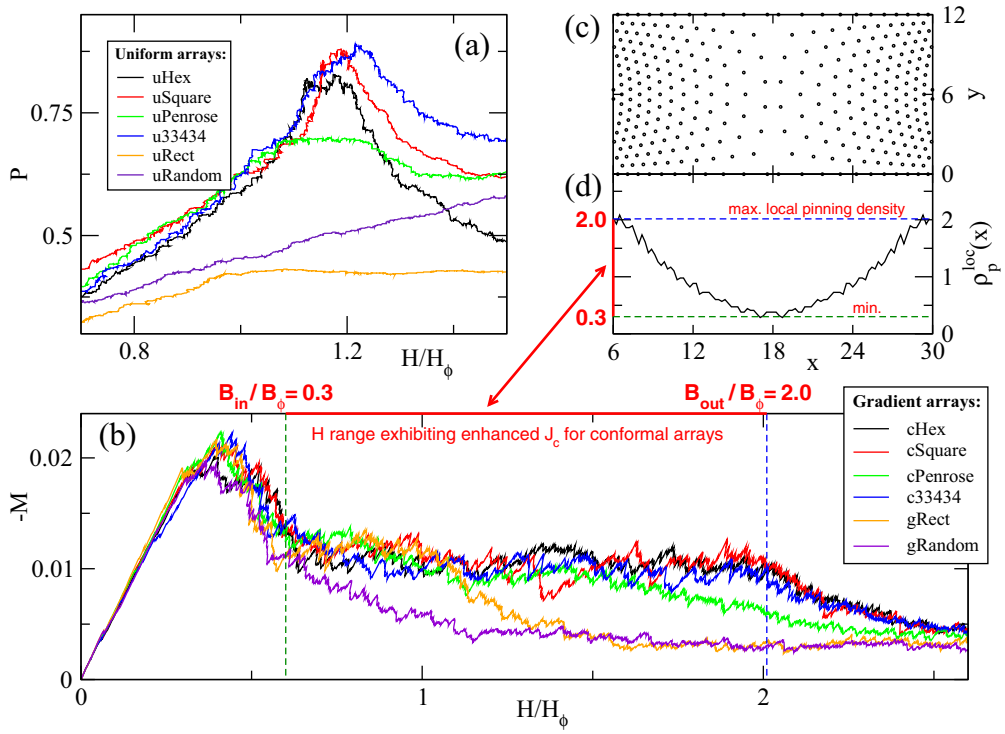

FIG. 11. (Color online) Local commensuration effects in conformal pinning arrays. (a) Spatially averaged fraction of occupied pins P vs H/H_ϕ in *uniform* arrays of (central peak, from top to bottom) hexagonal, square, Penrose, 33434, rectangular, and random type. Peaks in P just above $H/H_\phi = 1.0$ show that the hexagonal, square, Penrose, and 33434 arrays exhibit a robust matching effect. (b) Magnetization curves M vs H/H_ϕ for corresponding *gradient* pinning arrays (from upper left to lower left): cHex, cSquare, cPenrose, c33434, gRect, and gRandom. For the conformal arrays, the magnetization is enhanced whenever the vortex lattice can locally match with a vertical strip of the pinning array. (c) Spatial configuration of the pinning sites in a cHex array. (d) Corresponding local pinning density $\rho_p^{\rm loc}(x)$ for the same (cHex) array. The region between the dotted lines highlights the range of $\rho_p^{\rm loc}$ values existing somewhere inside the array. This range of possible local densities allowing matching [highlighted region in panel (d)] determines the range of applied fields [highlighted region in panel (b)] at which the conformal arrays provide enhanced values of M. The non-conformal gradient arrays do not enhance pinning by this mechanism.

VI. RECTANGULAR GRADIENT ARRAY AND COMMENSURATION EFFECTS

We next consider higher-field ordering and commensurability effects for the rectangular gradient or gRect pinning array, which were briefly noted in Fig. 5(c). In Fig. 12 we plot M versus H/H_ϕ for both the cHex and gRect arrays with $F_p = 0.9$, for fields up to $H/H_\phi = 5.2$. Here the effectiveness of the pinning for the conformal array clearly diminishes for fields above $H/H_\phi \approx 2.0$. The cHex array gives enhanced pinning compared to the gRect array for $1.0 \leqslant H/H_\phi \leqslant 2.5$. However, above this field range, M for the gRect array begins to increase dramatically and rises well above M for the cHex array, forming a broad peak centered at $H/H_\phi = 3.5$.

In Fig. 13(a), we plot M versus H/H_ϕ for rectangular gradient arrays with $F_p = 0.55$, 0.9, and 1.25, showing that the broad peak in M is a robust feature. In Fig. 13(b) we plot the corresponding fraction of sixfold-coordinated vortices P_6 versus H/H_ϕ, where $P_6 = (1/N_{vs}) \sum_{i=1}^{N_{vs}} \delta_{z_i,6}$. Here N_{vs} is the number of vortices within the pinned region, the coordination number z_i of vortex i is obtained from a Voronoi tesselation, and for a triangular lattice $P_6 = 1.0$. Figure 13(c) shows the corresponding fraction of fivefold-coordinated vortices P_5 versus H/H_ϕ. Due to the gradient in the sample, we generally find $P_7 \ll P_5$ since vortices are moving into less dense areas, so we do not show P_7. In Fig. 13(a), M increases with increasing F_p when $H/H_\phi \leqslant 1.0$, drops to a low value independent of F_p for $1.0 < H/H_\phi < 2.0$, and increases

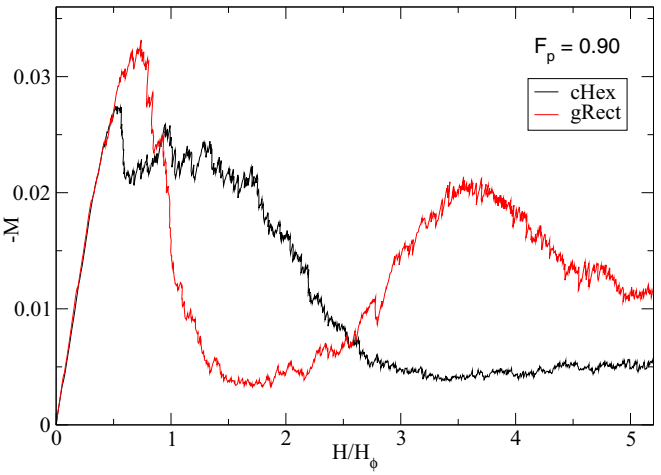

FIG. 12. (Color online) M vs H/H_ϕ for cHex (lower right) and gRect (upper right) samples with $F_p = 0.9$. Here the gRect array shows a commensuration peak near $H/H_\phi = 3.5$, where the magnetization is significantly enhanced compared to the cHex array.

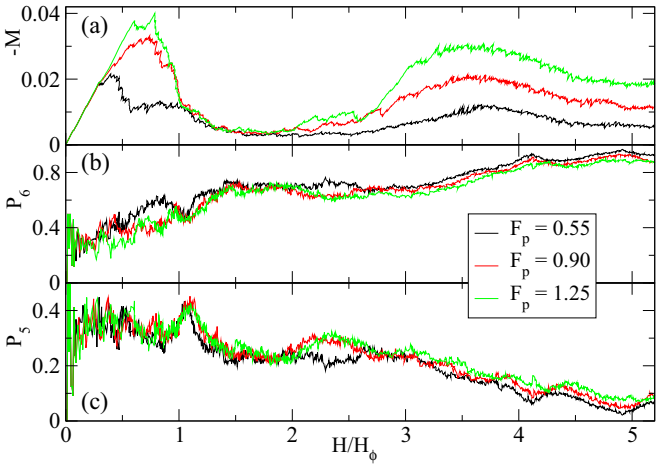

FIG. 13. (Color online) Results for the rectangular gradient array illustrated in Fig. 3(a). (a) M vs H/H_ϕ for $F_p = 1.25$ (upper curve), 0.9 (middle curve), and 0.55 (lowest curve). (b) The corresponding fraction of sixfold-coordinated vortices P_6 vs H/H_ϕ for $F_p = 1.25$ (lower right), 0.9 (middle right), and 0.55 (upper right). There is a small peak in P_6 near $H/H_\phi = 4.0$. (c) The corresponding fraction of fivefold-coordinated vortices P_5 vs H/H_ϕ for $F_p = 1.25$ (upper right), 0.9 (middle right), and 0.55 (lower right).

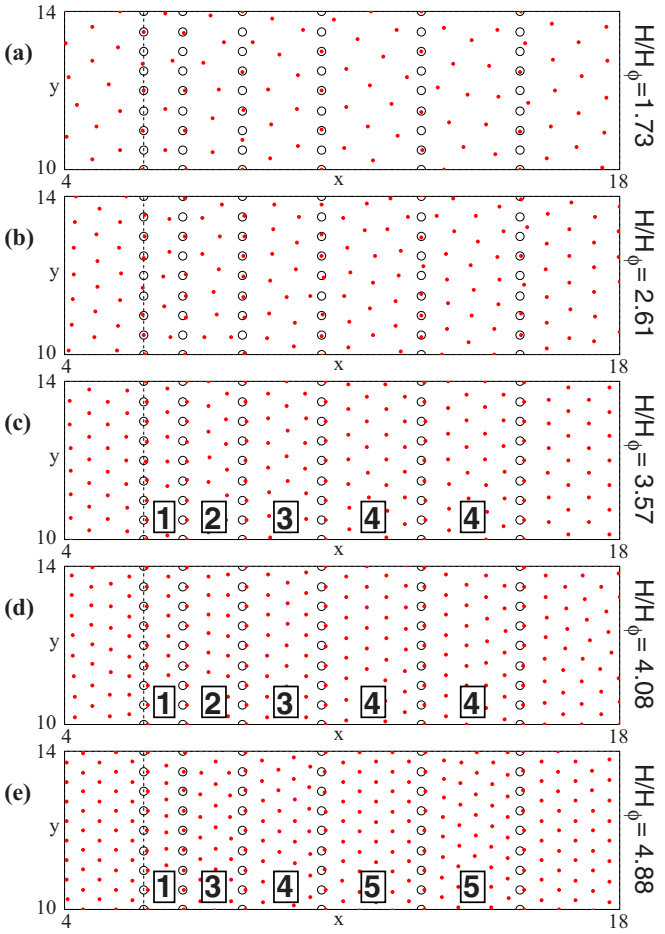

FIG. 14. (Color online) Ordered and disordered vortex states in rectangular gradient array with $F_p = 0.90$ at various values of H/H_ϕ. Filled circles: vortices; open circles: pinning sites. The dashed line on the left indicates the edge of the sample. (a) At $H/H_\phi = 1.73$, M reaches a minimum value and the vortices are disordered. (b) At $H/H_\phi = 2.61$, M increases and the number of occupied pins increases. (c) At $H/H_\phi = 3.57$, there is an ordered state corresponding to the peak in M in Fig. 13(a). The numbers indicate the number of ordered vortex columns between columns of pinning sites. (d) At $H/H_\phi = 4.08$, we observe an ordered state at the P_6 peak in Fig. 13(b). (e) At $H/H_\phi = 4.88$ we illustrate the ordered state at the second P_6 peak in Fig. 13(b).

with increasing F_p again for $2.0 \leqslant H/H_\phi$. For $H/H_\phi \lesssim 1.0$, vortices that enter the system tend to get captured by pinning sites, and the capture process is more efficient when F_p is higher. As in all computed magnetization curves irrespective of pinning geometry, the initial change in slope of M from positive to negative occurs at the field at which the vortices first reach the center of the sample; above this field, the vortices begin to enter the interstitial regions of the rectangular gradient array, where they encounter one-dimensional easy-flow channels oriented along the y direction, perpendicular to the gradient. The interstitial vortices, although unpinned, experience an effective pinning force due to caging by the surrounding pinned vortices. This effective force is not affected by an increase in F_p, which only traps the pinned vortices more firmly. Thus, in the field range $1.0 < H/H_\phi < 2.0$ where interstitial pinning is dominant, we find that the value of M is nearly independent of F_p. There is a dip in P_6 in Fig. 13(b) just above $H/H_\phi = 1.0$ and a corresponding peak in P_5 in Fig. 13(c), at the transition to the interstitial vortex regime.

For $H/H_\phi > 3.25$, Fig. 13 shows that P_6 begins to increase as M rises to a broad peak centered near $H/H_\phi = 3.75$. There is a small peak in P_6 near $H/H_\phi = 4.1$ followed by a small decrease in the region where M is also decreasing. The broad peak in M at these higher fields is due to a commensuration effect associated with the formation of ordered vortex chain structures, as illustrated in Fig. 14 where we show the vortex configurations in the gRect array for different field values. Figure 14(a) shows the configuration at $H/H_\phi = 1.73$, where there is a minimum in M in Fig. 13(a). Here the vortices are largely disordered, and substantial depinning has occurred as indicated by the large fraction of empty pinning sites. At $H/H_\phi = 2.61$ in Fig. 14(b), M begins to increase and the pinning sites fill, but there is still no clear ordering present. When M reaches its maximum at $H/H_\phi = 3.57$, Fig. 14(c) shows that the vortex configuration within the pinning array is now ordered. To highlight this ordering, we mark the number of vortex chains that fit between pinning columns in Fig. 14(c). Between the two leftmost columns, there is one chain of vortices; between the next two columns, there are two chains with the vortices forming a zigzag structure; between the next two columns, there are three chains forming a local triangular lattice, and similarly in the next two gaps there are four chains. Similar structures, but with different numbers of vortex chains in between pinning columns, appear in Fig. 14(d) at $H/H_\phi = 4.08$ where there is a peak in P_6 in Fig. 13(b), as well as at $H/H_\phi = 4.88$ in Fig. 14(e), where there is a second peak in P_6 in Fig. 13(b).

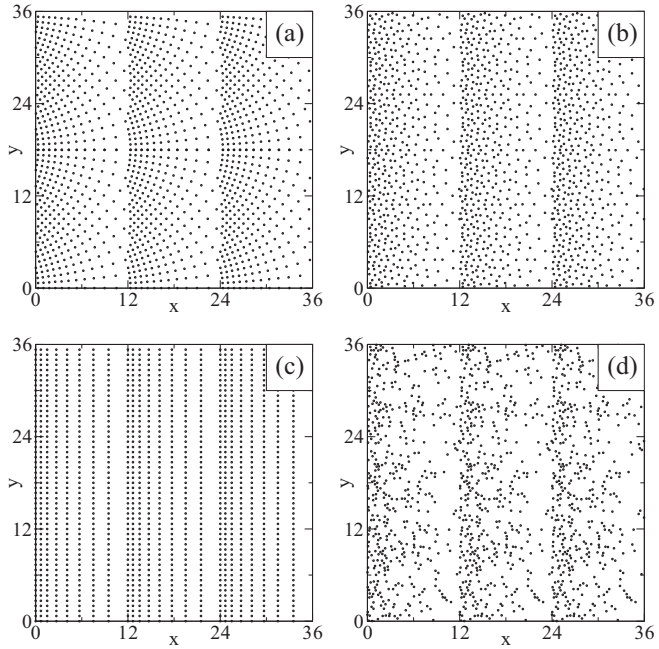

FIG. 15. Pinning geometries for current-driven simulations with various pinning arrays: (a) cSquare; (b) cPenrose; (c) gRect; (d) gRandom.

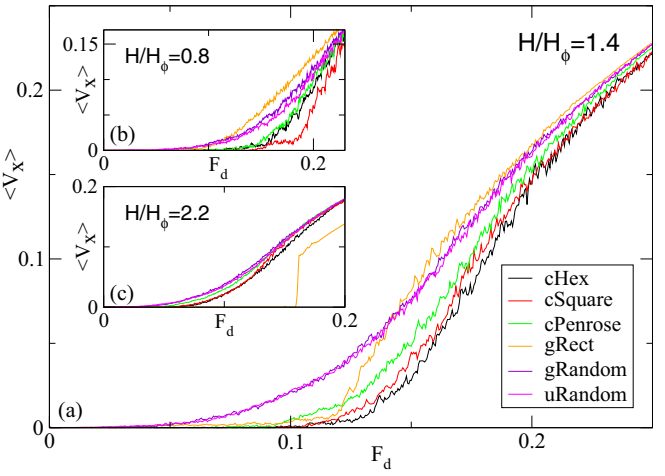

FIG. 16. (Color online) The average vortex velocity in the x direction $\langle V_x \rangle$ vs F_d for current-driven simulations of cHex, cSquare, cPenrose, gRect, gRandom, and uRandom transport arrays with $F_p = 0.55$ and a drive angle of $\theta = 0$ at different vortex densities. (a) $H/H_\phi = 1.4$ for cHex, cSquare, cPenrose, uRandom, gRandom, and gRect, from lower right to upper right. (b) $H/H_\phi = 0.8$ for cSquare, cHex, cPenrose, uRandom, gRandom, and gRect, from lower right to upper right. (c) $H/H_\phi = 2.2$ for gRect, cHex, cSquare, cPenrose, uRandom, and gRandom, from lower right to upper right. In general, the conformal arrays have a higher depinning threshold and lower vortex velocity than the nonconformal arrays. The gRect array exhibits a large depinning threshold at $H/H_\phi = 2.2$ due to a commensuration effect.

VII. CURRENT-DRIVEN RESULTS

In the previous sections, we studied vortex ordering and critical states using quasistatic flux gradient-driven simulations. To examine the vortex dynamics, we use current-driven simulations in which a steadily increasing drive is uniformly applied to the vortices in the sample. We consider driving directions that are aligned with the gradient (x) direction as well as drives oriented at some angle θ to this direction. The equations of motion for the current-driven simulations were described in Sec. III; the sample geometry is illustrated in Fig. 15.

A. Drive aligned with gradient

We first consider driving vortices along the gradient in the positive x direction. We define the driving angle θ as the angle the driving direction makes with the positive x axis, so that $\theta = 0$ corresponds to driving along the gradient direction. In Fig. 16(a) we plot $\langle V_x \rangle$ versus F_d for systems with $F_p = 0.55$, $\theta = 0$, and $H/H_\phi = 1.4$; we consider the cHex array shown in Fig. 4(b), the cSquare, cPenrose, gRect, and gRandom arrays shown in Fig. 15, and a uniform random array lacking any gradient. The depinning force F_c, defined as the magnitude of the drive above which $\langle V_x \rangle \geqslant 10^{-4}$, is significantly larger in the conformal arrays than in the nonconformal arrays. Additionally, in the moving phase the vortices travel more slowly through conformal arrays than through the nonconformal arrays over a substantial range of F_d. Among the conformal arrays, the cHex array gives the highest F_c, with F_c for the cSquare array almost as high and slightly smaller for the cPenrose array. At higher F_d the curves start to come together as the effectiveness of the pinning at the higher drives is washed out and $\langle V_x \rangle \approx F_d$. At a lesser field of $H/H_\phi = 0.8$, as shown in Fig. 16(b), $\langle V_x \rangle$ for the cSquare array drops below that of the cHex array at higher drives, indicating enhanced pinning effectiveness in the cSquare array, while the curves for the cHex and cPenrose arrays are very similar. The gRect array has the weakest pinning, followed by the random arrays with and without a gradient.

In Fig. 16(c) we illustrate the behavior at a higher field of $H/H_\phi = 2.2$. At this field, the gRect array exhibits a highly enhanced depinning force, followed by an abrupt transition to steady vortex motion. Inspection of the vortex configurations reveals that the vortices form an ordered vortex chain state of the type discussed in Sec. VI, which locks them into place and prevents vortex flow. Because our gRect transport and magnetization arrays have somewhat different configurations, they form these ordered states at different field levels; however, the qualitative behavior of gRect remains the same during transport, with the array exhibiting enhanced performance only when it is able to form vortex chain states. The difference between the conformal and nonconformal random arrays is somewhat reduced at $H/H_\phi = 2.2$, since this is above the cutoff field value of $H/H_\phi = 2.0$ where the conformal arrays start to exhibit decreased pinning effectiveness. The conformal arrays still perform better by giving higher values of F_c and lower values of $\langle V_x \rangle$ in the moving phase than the random arrays. The cSquare and cHex arrays have almost the same behavior, and are again superior to cPenrose.

These results are completely consistent with the results from our magnetization simulations. The transport simulations confirm that the pinning effectiveness is enhanced in conformal arrays over nonconformal ones, and the fact that the gRandom

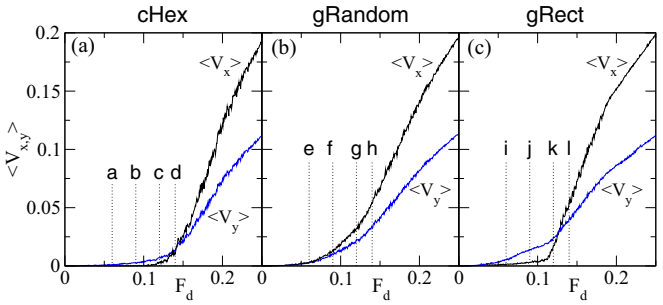

FIG. 17. (Color online) $\langle V_x \rangle$ and $\langle V_y \rangle$ vs F_d for current-driven systems with $F_p = 0.55$ at $H/H_\phi = 1.4$, driven at $\theta = 30^\circ$ with respect to the positive x axis. (a) cHex array; (b) gRandom array; (c) gRect array. The labeled current levels *a*-*l* correspond to the vortex trajectories illustrated in Fig. 18.

and uRandom arrays give nearly identical results indicates that it is not merely the gradient in the pinning that matters but also the local ordering. The precise type of local ordering is of lesser importance, although (as with magnetization) the quasiperiodic Penrose ordering is somewhat less effective at enhancing the pinning than periodic orderings.

B. Driving in different directions

Next we consider the effect of changing θ, the orientation of the driving direction, for various gradient pinning arrays. In Fig. 17 we plot the average velocity in the x direction $\langle V_x \rangle$ and y direction $\langle V_y \rangle$ as a function of F_d for the cHex, gRandom, and gRect arrays, at a drive angle of $\theta = 30^\circ$. For the cHex array in Fig. 17(a), $\langle V_y \rangle$ is nonzero for $0.05 < F_d < 0.10$ while $\langle V_x \rangle$ remains zero, meaning that vortex flow occurs strictly in the y direction, perpendicular to the gradient, even though the largest component of the external drive is along the x direction. Once the vortices start to move along the x direction as well, we find a crossing of the $\langle V_x \rangle$ and $\langle V_y \rangle$ curves near $F_d = 0.15$. In Figs. 18(a)–18(d) we illustrate the vortex flow in the cHex array at the drive values marked with the letters *a*–*d* in Fig. 17(a). At $F_d = 0.06$ and 0.09 in Figs. 18(a) and 18(b), the vortex flow occurs in winding rivers aligned with the y direction, which pass through the portions of the sample in which the pinning density is lowest. The cHex array exhibits a pronounced guidance or channeling effect since most of the pins are occupied in the higher pinning density regions, creating a barrier to vortex motion, while the local depinning threshold is reduced in areas of lower pinning density. At $F_d = 0.12$, Fig. 18(c) shows that vortices begin to cross between the easy flow channels, passing through the denser pinning region. This corresponds with the emergence of a nonzero value of $\langle V_x \rangle$ in Fig. 17(a) at point *c*. At higher drives the amount of motion in the x direction between easy-flow channels increases, as illustrated in Fig. 18(d) at $F_d = 0.14$.

For the random gradient array the depinning transition falls at a much lower value of F_d, as shown in Fig. 17(b), and unlike in the cHex array there is no vortex guidance effect in which flow only occurs in the y direction. Instead, $\langle V_x \rangle$ and $\langle V_y \rangle$ both increase smoothly with increasing F_d, and there is no crossing of the velocity curves. In Fig. 16 we showed that a random gradient array driven in the gradient direction with $\theta = 0^\circ$ has essentially identical transport properties to a uniform random array, indicating that the addition of a gradient to a random array does not substantially affect vortex flow. Similarly, we find that for $\theta \neq 0^\circ$ the flow through random arrays is also not affected by the addition of a gradient. In Figs. 18(e)–18(h) we show the vortex trajectories for the drives labeled *e*–*h* in Fig. 17. At $F_d = 0.06$ and 0.09 in Figs. 18(e) and 18(f), the vortices move in both the x and y directions and form winding channels oriented along the driving direction. Due to the less effective pinning in the gRandom array, the number of moving vortices is much greater than in the cHex array at the same drive, as can be seen by comparing the high trajectory densities in Figs. 18(e) and 18(f) to the much sparser trajectories in Figs. 18(a) and 18(b). At $F_d = 0.14$ in Fig. 18(h), most of the vortices are moving. At drives higher than those illustrated here, the vortices dynamically reorder in a manner similar to the dynamic reordering transitions observed for vortices driven over uniform random pinning arrays [64,65].

Figure 17(c) shows $\langle V_x \rangle$ and $\langle V_y \rangle$ versus F_d curves for the rectangular gradient array. Here there is a pronounced guidance effect for $0.02 < F_d < 0.11$; however, unlike in the cHex array, $\langle V_x \rangle$ is not strictly zero, indicating that some vortex motion is occurring in the x direction between the 1D columns of pins since the gRect array is less effective in restricting vortex motion along its gradient. The vortex flow images in Figs. 18(i)–18(l) correspond to the labeled drives in Fig. 17(c). For $F_d = 0.06$ and 0.09 in Figs. 18(i) and 18(j), the vortices follow nearly 1D paths along the y direction with very little winding, while there are a smaller number of flow channels oriented approximately parallel to the x direction that connect some of the 1D paths. The 1D vertical flow channels are concentrated in the least dense portions of the pinning array, and are similar in nature to the 1D flow of interstitial vortices observed in uniform square or rectangular periodic pinning arrays [66]. At $F_d = 0.12$ in Fig. 18(k), there is a significant increase in the amount of vortex flow along the x direction, while for $F_d = 0.14$ in Fig. 18(l) the flow is continuous through the system and oriented with the driving direction. As with the gRandom array, the high trajectory densities indicate pinning which is less effective than in the cHex array. For $F_d > 0.20$ the vortices dynamically order, as indicated by the onset of a linear regime of $\langle V_x \rangle$ versus F_d in Fig. 17(c).

We summarize the transport properties for different drive angles in Fig. 19, where we plot $\langle V_x \rangle$ and $\langle V_y \rangle$ versus θ for different values of F_d in the cHex and gRandom arrays. In the absence of pinning, we would obtain $\langle V_x \rangle = F_d \cos(\theta)$ and $\langle V_y \rangle = F_d \sin(\theta)$. For the cHex array with $F_d = 0.09$, shown in Fig. 19(a), $\langle V_x \rangle \approx 0$ for all θ, while $\langle V_y \rangle$ monotonically increases with increasing θ. This drive is too weak to depin the vortices along the x direction, but the vortices can flow in the y direction through the low density regions as was shown in Fig. 18(b). Figure 19(b) shows the same quantities for the gRandom array at the same drive $F_d = 0.09$. Here $\langle V_x \rangle$ is nonzero over the whole range of θ since the depinning threshold in the x direction is much lower for the gRandom array. There is an asymmetry in the x and y direction responses, as indicated by the fact that $\langle V_x \rangle = 0.015$ at $\theta = 0^\circ$ but $\langle V_y \rangle = 0.021$ at $\theta = 90^\circ$. This indicates that the pinning in the moving phase is slightly more effective

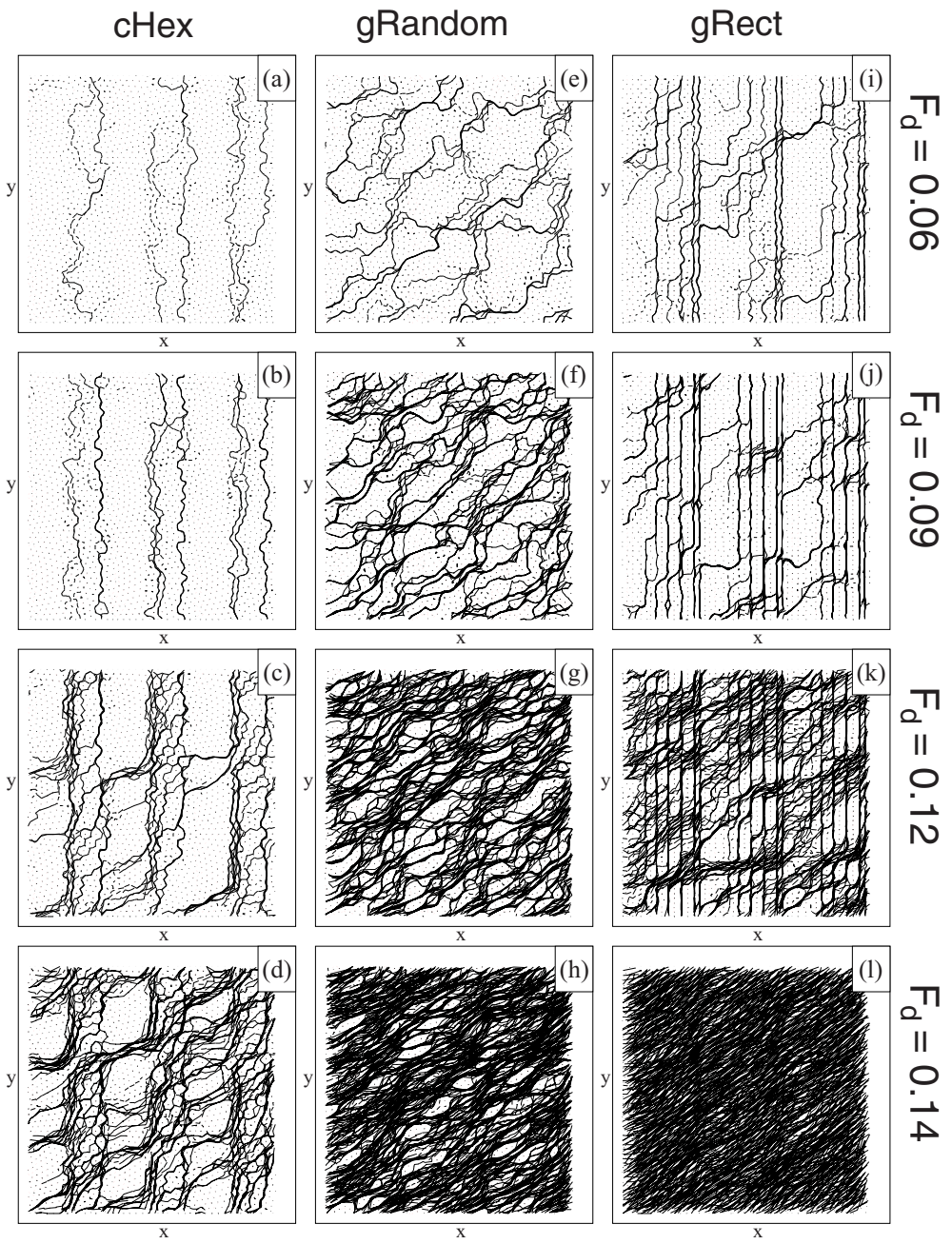

FIG. 18. (Color online) Lines: vortex trajectories; dark dots: vortex positions; and light dots: pin positions for selected values of F_d in the current-driven systems described in Fig. 17 with $F_p = 0.55$, $H/H_\phi = 1.4$, and drive orientation $\theta = 30^\circ$. (a)–(d) cHex; (e)–(h) gRandom; (i)–(l) gRect. F_d = [(a),(e),(i)] 0.06, [(b),(f),(j)] 0.09, [(c),(g),(k)] 0.12, and [(d),(h),(l)] 0.14.

when the vortices are moving along the gradient direction. However, the vortex velocities are much larger in the gRandom array than in the cHex array over the whole range of θ, showing the robust enhanced effectiveness of the conformal pinning.

When the drive in the cHex array is increased to $F_d = 0.14$, Fig. 19(c) shows that the x direction depinning threshold is exceeded for $\theta < 70^\circ$, but that the vortex motion along the x direction is still greatly suppressed even when the vortices are flowing. There is still a strong vortex channeling effect in the y direction, as reflected in the large asymmetry between $\langle V_x\rangle(\theta)$ and $\langle V_y\rangle(90^\circ - \theta)$. For the gRandom array at $F_d = 0.14$, Fig. 19(d) indicates that this drive magnitude is already large enough to render the pinning mostly ineffective, as also shown in Fig. 18(h). The $\langle V_x\rangle$ and $\langle V_y\rangle$ curves are almost mirror symmetric, indicating that the pinning gradient has little effect on the motion of the vortices. At $F_d = 0.20$, Fig. 19(e) shows that the response of cHex becomes increasingly symmetrical, although there is still a small channeling regime for $\theta \geqslant 80^\circ$ where the flow is strictly confined along the y direction. At higher drives (not shown), the $\langle V_x\rangle$ and $\langle V_y\rangle$ curves for cHex become symmetric. For the gRandom array at $F_d = 0.20$, Fig. 19(f) indicates that the response is almost completely symmetrical.

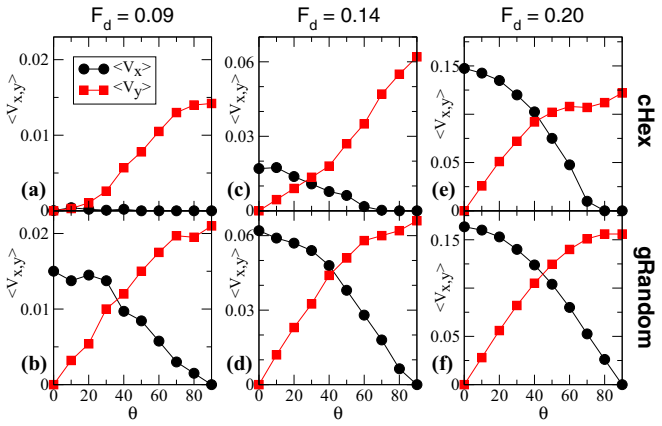

FIG. 19. (Color online) $\langle V_x \rangle$ (circles) and $\langle V_y \rangle$ (squares) vs drive angle θ for the cHex [(a),(c),(e)] and gRandom [(b),(d),(f)] arrays, at $F_d = 0.09$ [(a),(b)], $F_d = 0.14$ [(c),(d)], and $F_d = 0.20$ [(e),(f)]. We fix $F_p = 0.55$ and $H/H_\phi = 1.4$.

VIII. SUMMARY

We have investigated the magnetization, ordering, and transport for vortices interacting with pinning arrays where there is a gradient in the pinning density. We consider conformal pinning arrays constructed by taking a conformal transformation of a uniform pinning array; the new structure has a density gradient but preserves certain crystalline topological features of the original lattice. In particular, we examine conformal crystals obtained from uniform hexagonal, square, Archimedean, and quasiperiodic arrays. We also investigate selected nonconformal arrays with a pinning gradient, including a rectangular pinning array with a 1D gradient and a random arrangement of pinning sites with a gradient. In general we find that conformal arrays which are transformed versions of uniform pinning with well-defined commensurability peaks give the strongest pinning over the widest range of fields. The hexagonal and square conformal arrays produce the strongest pinning and highest critical currents, followed by the conformal Archimedean and conformal Penrose arrays. The random gradient array gives only a slight enhancement in pinning over a uniform random array, indicating that it is the preservation of the local periodicity in the conformal transformation combined with the gradient that gives rise to the enhanced pinning. We show that for the conformal crystal arrays, a portion of the vortices in the sample is locally commensurate with a portion of the pinning array, and this local commensuration effect gradually moves through the system as the externally applied magnetic field is changed. When the field becomes high enough that the vortex density exceeds the pinning density at the outer edge of the sample, the effectiveness of the conformal arrays breaks down, although they still show a small enhancement in pinning compared to random arrays. The rectangular gradient pinning array has relatively weak pinning compared to the conformal arrays at lower fields; however, for higher fields, it develops a pronounced broad peak due to a novel commensuration effect in which integer numbers of ordered columns of vortices fit between the columns of pinning sites.

We also show that the enhanced pinning by the conformal arrays can be observed in current-driven transport measurements. Compared to uniform random or random gradient arrays, the conformal arrays have higher critical depinning forces, and lower average vortex velocities in the moving phase. When the vortices are driven at different angles with respect to the gradient direction, the conformal arrays guide vortex flow perpendicular to the gradient, in channels that pass through the regions of lower pinning density. The rectangular gradient array exhibits a similar guidance effect, with a strongly 1D flow of vortices in the interstitial regions.

In this work we focus on vortices in gradient arrays; however, we expect similar results for other systems featuring particles moving over substrates where the substrate has some type of gradient.

ACKNOWLEDGMENTS

We thank Boldizsár Jankó for useful discussions. This work was carried out under the auspices of the NNSA of the US DOE at LANL under Contract No. DE-AC52-06NA25396.

[1] G. Blatter, M. V. Feigelman, V. B. Geshkenbein, A. I. Larkin, and V. M. Vinokur, Rev. Mod. Phys. **66**, 1125 (1994).
[2] G. Grüner, Rev. Mod. Phys. **60**, 1129 (1988).
[3] V. J. Goldman, M. Santos, M. Shayegan, and J. E. Cunningham, Phys. Rev. Lett. **65**, 2189 (1990); G. A. Csáthy, D. C. Tsui, L. N. Pfeiffer, and K. W. West, *ibid.* **98**, 066805 (2007).
[4] A. Vanossi, N. Manini, M. Urbakh, S. Zapperi, and E. Tosatti, Rev. Mod. Phys. **85**, 529 (2013).
[5] S. Xia, L. Ponson, G. Ravichandran, and K. Bhattacharya, Phys. Rev. Lett. **108**, 196101 (2012).
[6] D. Ravelosona, D. Lacour, J. A. Katine, B. D. Terris, and C. Chappert, Phys. Rev. Lett. **95**, 117203 (2005).
[7] A. Vanossi, N. Manini, and E. Tosatti, Proc. Natl. Acad. Sci. USA **109**, 16429 (2012); D. McDermott, J. Amelang, C. J. Olson Reichhardt, and C. Reichhardt, Phys. Rev. E **88**, 062301 (2013).
[8] M. Baert, V. V. Metlushko, R. Jonckheere, V. V. Moshchalkov, and Y. Bruynseraede, Phys. Rev. Lett. **74**, 3269 (1995).
[9] K. Harada, O. Kamimura, H. Kasai, T. Matsuda, A. Tonomura, and V. V. Moshchalkov, Science **274**, 1167 (1996).
[10] S. Goldberg, Y. Segev, Y. Myasoedov, I. Gutman, N. Avraham, M. Rappaport, E. Zeldov, T. Tamegai, C. W. Hicks, and K. A. Moler, Phys. Rev. B **79**, 064523 (2009).
[11] I. Swiecicki, C. Ulysse, T. Wolf, R. Bernard, N. Bergeal, J. Briatico, G. Faini, J. Lesueur, and J. E. Villegas, Phys. Rev. B **85**, 224502 (2012); R. Cordoba *et al.*, Nat. Commun. **4**, 1437 (2013).
[12] J. I. Martín, M. Velez, J. Nogues, and I. K. Schuller, Phys. Rev. Lett. **79**, 1929 (1997); C. Chiliotte, G. Pasquini, V. Bekeris, J. E.

Villegas, C.-P. Li, and I. K. Schuller, Supercond. Sci. Technol. **24**, 065008 (2011).
[13] U. Welp, X. L. Xiao, V. Novosad, and V. K. Vlasko-Vlasov, Phys. Rev. B **71**, 014505 (2005).
[14] C. J. Olson, C. Reichhardt, and F. Nori, Phys. Rev. B **56**, 6175 (1997).
[15] C. Reichhardt, C. J. Olson, and F. Nori, Phys. Rev. B **57**, 7937 (1998).
[16] C. Reichhardt, G. T. Zimányi, R. T. Scalettar, A. Hoffmann, and I. K. Schuller, Phys. Rev. B **64**, 052503 (2001).
[17] G. R. Berdiyorov, M. V. Milosevic, and F. M. Peeters, Phys. Rev. Lett. **96**, 207001 (2006); Phys. Rev. B **74**, 174512 (2006).
[18] C. Reichhardt and N. Grønbech-Jensen, Phys. Rev. B **63**, 054510 (2001).
[19] S. B. Field, S. S. James, J. Barentine, V. Metlushko, G. Crabtree, H. Shtrikman, B. Ilic, and S. R. J. Brueck, Phys. Rev. Lett. **88**, 067003 (2002); A. N. Grigorenko, S. J. Bending, M. J. Van Bael, M. Lange, V. V. Moshchalkov, H. Fangohr, and P. A. J. de Groot, *ibid.* **90**, 237001 (2003).
[20] J. I. Martín, M. Vélez, A. Hoffmann, I. K. Schuller, and J. L. Vicent, Phys. Rev. Lett. **83**, 1022 (1999); Ajay D. Thakur, S. Ooi, M. Chand, J. Jesudasan, P. Raychaudhuri, and K. Hirata, *Solid State Physics*, AIP Conf. Proc. No. 1591 (AIP, Melville, NY, 2014), p. 1651.
[21] M. Vélez, J. I. Martín, J. E. Villegas, A. Hoffmann, E. M. González, J. L. Vicent, and I. K. Schuller, J. Magn. Magn. Mater. **320**, 2547 (2008).
[22] C. Reichhardt, G. T. Zimányi, and N. Grønbech-Jensen, Phys. Rev. B **64**, 014501 (2001).
[23] G. Karapetrov, J. Fedor, M. Iavarone, D. Rosenmann, and W. K. Kwok, Phys. Rev. Lett. **95**, 167002 (2005).
[24] C. J. Olson Reichhardt, A. Libál, and C. Reichhardt, Phys. Rev. B **73**, 184519 (2006).
[25] T. C. Wu, J. C. Wang, Lance Horng, J. C. Wu, and T. J. Yang, J. Appl. Phys. **97**, 10B102 (2005).
[26] C. Reichhardt and C.J. Olson Reichhardt, Phys. Rev. B **76**, 064523 (2007).
[27] C. Reichhardt and C.J. Olson Reichhardt, Phys. Rev. Lett. **100**, 167002 (2008).
[28] M. L. Latimer, G. R. Berdiyorov, Z. L. Xiao, W. K. Kwok, and F. M. Peeters, Phys. Rev. B **85**, 012505 (2012).
[29] C. Reichhardt and C. J. Olson Reichhardt, Phys. Rev. B **76**, 094512 (2007).
[30] M. Kemmler, D. Bothner, K. Ilin, M. Siegel, R. Kleiner, and D. Koelle, Phys. Rev. B **79**, 184509 (2009).
[31] Y. J. Rosen, A. Sharoni, and I. K. Schuller, Phys. Rev. B **82**, 014509 (2010).
[32] C. J. Olson Reichhardt and C. Reichhardt, Phys. Rev. B **81**, 224516 (2010).
[33] N. S. Lin, T. W. Heitmann, K. Yu, B. L. T. Plourde, and V. R. Misko, Phys. Rev. B **84**, 144511 (2011).
[34] G. Karapetrov, V. Yefremenko, G. Mihajlović, J. E. Pearson, M. Iavarone, V. Novosad, and S. D. Bader, Phys. Rev. B **86**, 054524 (2012).
[35] K. Yu, M. B. S. Hesselberth, P. H. Kes, and B. L. T. Plourde, Phys. Rev. B **81**, 184503 (2010).
[36] A. Libál, C. J. Olson Reichhardt, and C. Reichhardt, Phys. Rev. Lett. **102**, 237004 (2009).
[37] M. L. Latimer, G. R. Berdiyorov, Z. L. Xiao, F. M. Peeters, and W. K. Kwok, Phys. Rev. Lett. **111**, 067001 (2013).
[38] J. Trastoy, M. Malnou, C. Ulysse, R. Bernard, N. Bergeal, G. Faini, J. Lesueur, J. Briatico, and J. E. Villegas, Nat. Nanotechn., doi:10.1038/nnano.2014.158.
[39] A. V. Silhanek, L. Van Look, R. Jonckheere, B. Y. Zhu, S. Raedts, and V. V. Moshchalkov, Phys. Rev. B **72**, 014507 (2005).
[40] R. Cao, Lance Horng, T. J. Yang, T. C. Wu, J. C. Wang, and J. C. Wu, J. Appl. Phys. **107**, 09E129 (2010).
[41] A. Kiliç, K. Kiliç, M. Olutaş, and A. Altinkok, Eur. Phys. J. B **86**, 339 (2013).
[42] V. R. Misko, S. Savelev, and F. Nori, Phys. Rev. Lett. **95**, 177007 (2005); Phys. Rev. B **74**, 024522 (2006).
[43] A. V. Silhanek, W. Gillijns, V. V. Moshchalkov, B. Y. Zhu, J. Moonens, and L. H. A. Leunissen, Appl. Phys. Lett. **89**, 152507 (2006).
[44] J. E. Villegas, M. I. Montero, C.-P. Li, and I. K. Schuller, Phys. Rev. Lett. **97**, 027002 (2006).
[45] M. Kemmler, C. Gurlich, A. Sterck, H. Pöhler, M. Neuhaus, M. Siegel, R. Kleiner, and D. Koelle, Phys. Rev. Lett. **97**, 147003 (2006).
[46] R. B. G. Kramer, A. V. Silhanek, J. Van de Vondel, B. Raes, and V. V. Moshchalkov, Phys. Rev. Lett. **103**, 067007 (2009).
[47] V. R. Misko, D. Bothner, M. Kemmler, R. Kleiner, D. Koelle, F. M. Peeters, and F. Nori, Phys. Rev. B **82**, 184512 (2010).
[48] C. Reichhardt and C. J. Olson Reichhardt, Phys. Rev. Lett. **106**, 060603 (2011).
[49] D. Ray, C. J. Olson Reichhardt, B. Jankó, and C. Reichhardt, Phys. Rev. Lett. **110**, 267001 (2013).
[50] P. Pieranski, in *Phase Transitions in Soft Condensed Matter*, edited by T. Riste and D. Sherrington (Plenum, New York, 1989), p. 45; F. Rothen, P. Pieranski, N. Rivier, and A. Joyet, Eur. J. Phys. **14**, 227 (1993); F. Rothen and P. Pieranski, Phys. Rev. E **53**, 2828 (1996).
[51] D. Ray, C. Reichhardt, C. J. Olson Reichhardt, and B. Jankó, Physica C **503**, 123 (2014).
[52] Y. L. Wang, M. L. Latimer, Z. L. Xiao, R. Divan, L. E. Ocola, G. W. Crabtree, and W. K. Kwok, Phys. Rev. B **87**, 220501(R) (2013).
[53] S. Guénon, Y. J. Rosen, A. C. Basaran, and I. K. Schuller, Appl. Phys. Lett. **102**, 252602 (2013).
[54] M. Motta, F. Colauto, W. A. Ortiz, J. Fritzsche, J. Cuppens, W. Gillijns, V. V. Moshchalkov, T. H. Johansen, A. Sanchez, and A. V. Silhanek, Appl. Phys. Lett. **102**, 212601 (2013).
[55] V. R. Misko and F. Nori, Phys. Rev. B **85**, 184506 (2012).
[56] D. Ray, C. Reichhardt, and C. J. Olson Reichhardt, Supercond. Sci. Technol. **27**, 075006 (2014).
[57] B. Grünbaum and G. C. Shephard, *Tilings and Patterns* (W. H. Freeman, New York, 1987).
[58] See, for example, Z. Nehari, *Conformal Mapping* (Dover, New York, 1975).
[59] See, for example, *Quasicrystals: An Introduction to Structure, Physical Properties, and Applications*, edited by J.-B. Suck, M. Schrieber, and P. Häussler (Springer, Berlin, 2002).
[60] C. Reichhardt, C. J. Olson, J. Groth, S. Field, and F. Nori, Phys. Rev. B **52**, 10441 (1995); **53**, R8898(R) (1996).
[61] C. Reichhardt, J. Groth, C. J. Olson, S. B. Field, and F. Nori, Phys. Rev. B **54**, 16108 (1996).
[62] C. P. Bean, Phys. Rev. Lett. **8**, 250 (1962); Rev. Mod. Phys. **36**, 31 (1964).

[63] C. Reichhardt, C. J. Olson, and F. Nori, Phys. Rev. Lett. **78**, 2648 (1997).

[64] A. E. Koshelev and V. M. Vinokur, Phys. Rev. Lett. **73**, 3580 (1994); M. C. Faleski, M. C. Marchetti, and A. A. Middleton, Phys. Rev. B **54**, 12427 (1996).

[65] C. J. Olson, C. Reichhardt, and F. Nori, Phys. Rev. Lett. **81**, 3757 (1998).

[66] C. Reichhardt and C. J. Olson Reichhardt, Phys. Rev. B **79**, 134501 (2009); J. Gutierrez, A. V. Silhanek, J. Van de Vondel, W. Gillijns, and V. V. Moshchalkov, *ibid.* **80**, 140514 (2009).